



Slurry Erosion Behavior of HVOF-Sprayed WC-10Co-4Cr Coated SS 316 Steel with and Without PTFE Modification

Anuj Bansal¹ · Jagtar Singh¹ · Harpreet Singh²

Submitted: 18 April 2019 / in revised form: 30 July 2019 / Published online: 19 August 2019
© ASM International 2019

Abstract Several hydro-machinery components such as impellers of the submersible pump and turbine blades generally suffer from slurry erosion during their operation. High-velocity oxy-fuel (HVOF)-sprayed coatings are promising materials to prevent such components from slurry erosion. Moreover, polytetrafluoroethylene (PTFE) is a well-accepted hydrophobic material, which has several attractive properties such as chemical inertness and considerable thermal stability. Therefore, PTFE coating has been explored as a topcoat for a HVOF-sprayed WC-10Co-4Cr coating, with an aim to enhance the performance of the latter and analyzed with different slurry erosion conditions. A slurry erosion test rig was used for experimentation, and the effect of four different erosion parameters, namely average particle size, slurry concentration, impact angle, and velocity of jet, was investigated. A comparative study between PTFE-modified HVOF-sprayed coating and the standalone HVOF-sprayed coating was also done with respect to slurry erosion behavior and hydrophobicity. The overall results indicate that the slurry erosion of the HVOF-sprayed coated SS 316 steel got enhanced after modification by PTFE topcoat. Furthermore, the topcoat of PTFE on HVOF-sprayed coating resulted in a remarkable improvement in hydrophobicity, showing a superhydrophobic behavior, which might have also provided a better slurry erosion resistance to the HVOF-sprayed steel.

Keywords hydrophobicity · hydro-machinery steel · PTFE · slurry erosion · thermal spray coatings

Introduction

Submersible pumps are widely used for irrigation purpose in Northern India. Impellers and casings are the most critical components of these submersible pumps. These impellers are more prone to the slurry erosion (SE) as they are directly exposed to the slurry (water mixed with sand particles) during their operation. Due to slurry erosion, material from solid surface not only gets plowed but also may result into bulk failure (Ref 1, 2). Out of the different type of submersible pumps, the cavity bore submersible pumps are preferred due to the better quality of water delivered by them. However, the slurry erosion has been reported to be more severe in case of cavity bore submersible pump due to the presence of higher amount of finer sand particles in the water. This causes frequent replacement of the impellers, even twice a year, leading to a significant financial loss to the farmers' community. Similarly, in hydraulic turbines of hydro-power plants, components such as guide vanes, top and bottom ring liners, labyrinths, runner blades, and inlet valve seals also suffer from SE problem (Ref 3-6). SS 316 is a commonly used material for such components, which during prolonged exposure to the slurry erosion conditions gets eroded and losses its functionality. Slurry erosion depends on the shape and hardness of the erodent particles (Ref 7). Besides the hardness and shape of the erodent particles, the impingement conditions like impact velocity, angle of contact, concentration, and particle size also play a major role in slurry erosion (Ref 2, 8-12). It has been reported that the slurry erosion and erosion-corrosion (EC) of

✉ Anuj Bansal
anujbansalsliet@gmail.com

¹ Sant Longowal Institute of Engineering and Technology,
Longowal, Sangrur, Punjab 148106, India

² Indian Institute of Technology Ropar, Rupnagar,
Punjab 140001, India

components exposed to slurry are very common phenomena and cannot be completely eliminated, but can be controlled (Ref 13). In this regard, many researchers have tried different types of coating techniques and coating compositions to coat such fluid machinery components to reduce their slurry erosion (Ref 2-4, 6, 10, 14-18). Thermal spraying is one of most prominent categories of coating deposition processes in this context. Moreover, among different thermal spray coating processes, high-velocity oxy-fuel (HVOF) spray process has been found to be very promising process for such applications (Ref 4, 6, 14). Using HVOF-spray process, WC-based coatings have been extensively explored, among which WC-Co-Cr coatings have shown a remarkable resistance against slurry erosion (Ref 4, 6, 19, 20).

On the other side, after the discovery of the unique self-cleaning properties of the lotus leaf by Barthlott and Neinhuis (Ref 21), an extensive research is under progress on superhydrophobic bio-inspired artificial non-wettable surfaces. These surfaces are fabricated using different techniques such as laser texturing, etching, layer-by-layer assembly, CVD, nanocoatings, and lithography (Ref 22-34). When a liquid droplet is placed on such surfaces, it formulates into an almost spherical shape and subsequently rattle-off with a slight tilt of surface. Due to the phenomenal potential of super hydrophobic surfaces, these are incorporated in a vast number of applications (Ref 35, 36). But, in general, most superhydrophobic surfaces are very delicate in nature, and this limits the use of such surface in hydro-machinery components like impellers and guide vanes, etc. In this context, there has been an increased scientific effort recently toward significantly improving the mechanical performance of non-wettable surfaces (Ref 37, 38). A review article regarding the mechanical durability of superhydrophobic coatings was published in 2011 (Ref 38). Further, in 2016, a review article emphasized on various methods and tests used to investigate mechanical durability of such surfaces (Ref 37). In this regard, a method is reported by Chen et al. (Ref 39), in which a topcoat of a hydrophobic material on plasma sprayed silica surface resulted in a mechanically durable superhydrophobic surface (Ref 40). Different polymers are available as hydrophobic materials, among these polymers; polytetrafluoroethylene (PTFE) is well accepted as a hydrophobic material due to its several attractive properties such as chemical inertness, very low friction, and considerable thermal stability (Ref 28, 39-43). Therefore, PTFE coating has been explored as a topcoat for a HVOF coated SS 316, with an aim to enhance the performance of the latter. In the present work, a topcoat of PTFE was deposited on an already HVOF-sprayed WC-10Co-4Cr coating and analyzed with respect to different slurry erosion conditions. This study shall provide useful information

regarding the erosion performance of PTFE-modified HVOF-spray WC-10Co-4Cr coating on SS 316. A slurry erosion test rig was used for experimentation, and the effect of four different erosion parameters, namely average particle size, slurry concentration, impact angle, and velocity of jet, was investigated. A comparative study of PTFE-modified HVOF coating vis-à-vis the standalone HVOF coating was also done with respect to slurry erosion behavior and hydrophobicity.

Experimental Details

Base Material

SS 316 austenitic steel is a commonly used material for impellers of submersible pumps and other hydro-machinery components, which provides good toughness due to its austenite structure (Ref 44). Therefore, SS 316 was selected as a substrate material in the present research work. The raw material was procured in the form of forged rod of 25 mm diameter, and for validation of its composition, spectroscopy was conducted. The results obtained were in accordance with the standard composition of the material. The detailed chemical composition of the steel as obtained from the spectroscopy test is shown in Table 1. The specific mass and average microhardness of the steel was found to be 7.8 g/cc and 273.60 HV, respectively. Solid cylindrical samples of 25 mm diameter and 5 mm thickness were prepared from the steel.

Coating Deposition

Widely available WC-10Co-4Cr powder was sprayed on the SS 316 substrate using HVOF-spray technique. Further, a topcoat of PTFE was deposited on the already HVOF-sprayed WC-10Co-4Cr coating. The scanning electron microscope (SEM JEOL, JSM-6510LV) micrographs and energy-dispersive spectroscopy (EDS) data of the WC-10Co-4Cr and PTFE powders are shown in Fig. 1(a) and (b), respectively.

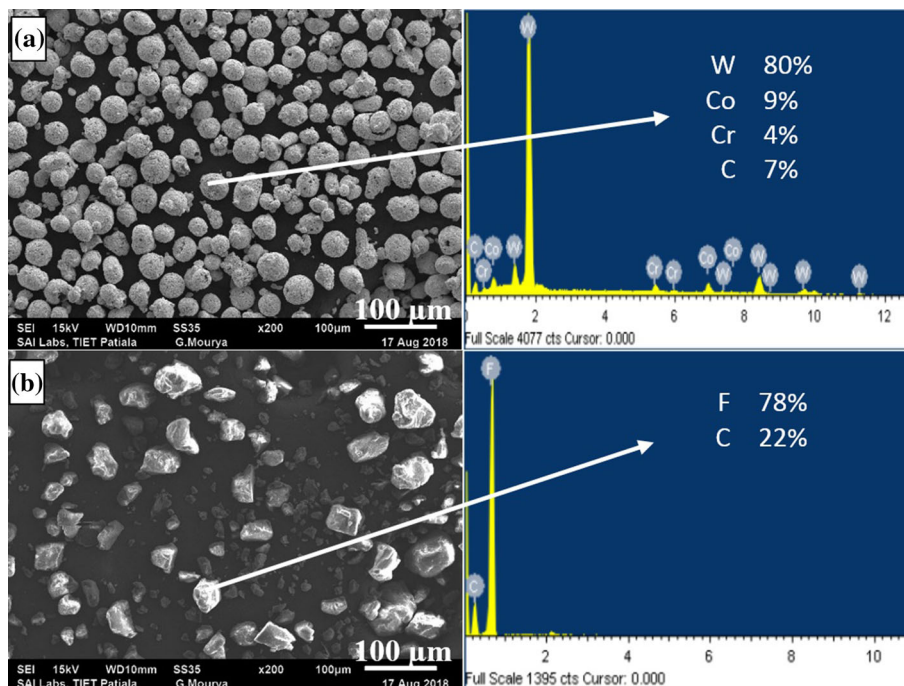
It can be observed from SEM micrograph that WC-10Co-4Cr particles exhibit an agglomerated sintered and spherical morphology with an average particle size of 25 μm , whereas PTFE particles seem to exhibit mixed morphology of round, ellipsoid and elongated particles with an average particle size of 40 μm (Ref 2, 6, 45). Further, EDS analysis verifies the presence of various elements in the powders, as per their chemical compositions. HVOF-sprayed coating work was performed at M/S Metallizing Equipment Company Private Limited, Jodhpur (India), using HIPOJET 2700 system. Before applying the HVOF coating, the uncoated specimens were grit blasted

Table 1 Chemical composition of SS 316

Elements	Carbon	Chromium	Manganese	Phosphorous	Sulfur	Silicon	Molybdenum	Iron
wt. %	0.0735	17.35	1.825	0.036	0.029	0.937	2.28	Balance

Table 2 Process parameter used for HVOF-sprayed coating

Parameter	Oxygen flow rate	Oxygen pressure	Fuel (LPG) flow rate	Fuel pressure	Air flow rate	Air pressure	Spray distance	Powder feed rate
Value	250-270 slpm	10.0 kg/cm ²	55-65 slpm	6.5-7.0 kg/cm ²	700-750 slpm	6.0-6.5 kg/cm ²	18 cm	40 g/min

Fig. 1 SEM micrograph and EDS analysis of (a) WC-10Co-4Cr and (b) PTFE powder

using Virgin Brown alumina oxide powder (GRIT 45) at a pressure of 2-5 kg/cm² to obtain the surface roughness of 8-9 μm for better coating adhesion, as per studies of the HVOF coatings performed by Goyal et al. (Ref 6). The process parameters used for HVOF-spray coating are shown in Table 2. The PTFE coating was performed at Coatec India, Sahibzada Ajit Singh Nagar, Punjab (India). The coating of PTFE was done on the surface using the already standardized process, as opted by the industry. According to the deposition process, PTFE dispersion (455G-01391) was applied on HVOF-sprayed samples, which acts as a binder for the PTFE powder. The samples were cleaned using acetone and dried before applying the primer.

Later, the PTFE powder from DuPont was sprayed on the dispersed surface followed by sintering. Sintering consisted of heating the samples to 385 °C at the rate of 80 °C per hour and holding the samples at the said temperature for half an hour followed by cooling to room

temperature in the furnace. In collaboration with the industry, different PTFE coatings were performed under different levels of sintering parameters. Based upon these iterations, the parameters constituting of heating temperature as 385 °C, heating rate as 80 °C per hour, and soaking period as half an hour were found to be best levels for a sound PTFE coating with 62 μm thickness, which was further found optimal for a minimum erosion, as observed from preliminary tests. Figure 2 shows the samples of PTFE-modified HVOF-sprayed WC-10Co-4Cr coating (hereafter referred as coating B), HVOF-sprayed WC-10Co-4Cr coating (hereafter referred as coating A), and bare steel (hereafter referred as SS 316) along with a schematic diagram for the coatings.

Sand for Slurry

The sand for the slurry erosion testing was collected from the three different field bores located in the Sangrur district

of Punjab, so as to simulate the practical conditions during the test. The collected sand was first dried under the Sun, and then, sieve analysis was performed on a Vibratory Sand Siever to characterize the particle size distribution (PSD). The sand with particle size more than 850 microns was discarded, so as to simulate the practical conditions during the test, as due to sand filters present in case of submersible pumps, the sand particles having size ≥ 850 microns are not permitted to reach the impellers. Further, three separate sets with different average particle sizes (150, 300, and 450 μm) were prepared by mixing the predetermined sizes of sand particles as shown in Fig. 3.

The SEM micrographs and EDS of the sand particles having different average particle size (150 μm , 300 μm , and 450 μm) are shown in Fig. 4. From the EDS analysis, it was observed that Fe, Si, Al, and O are the major constituents in the actual sand, which imply the presence of SiO_2 , Fe_2O_3 , and Al_2O_3 compounds in the sand.

Characterization of Coating

To analyze the thickness of coating A and coating B, the cross-sectional micrographs of both the coatings were taken by using an inverted trinocular microscope,

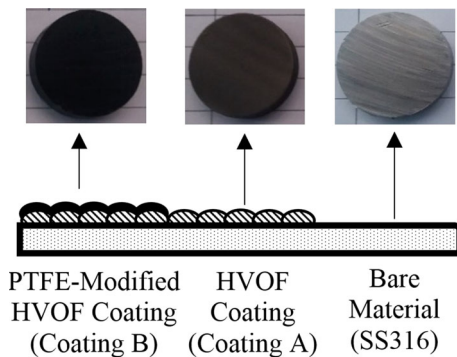


Fig. 2 Samples of PTFE-modified HVOF-sprayed WC-10Co-4Cr coating (coating B), standalone HVOF-sprayed WC-10Co-4Cr coating (coating A), and bare steel (SS 316)

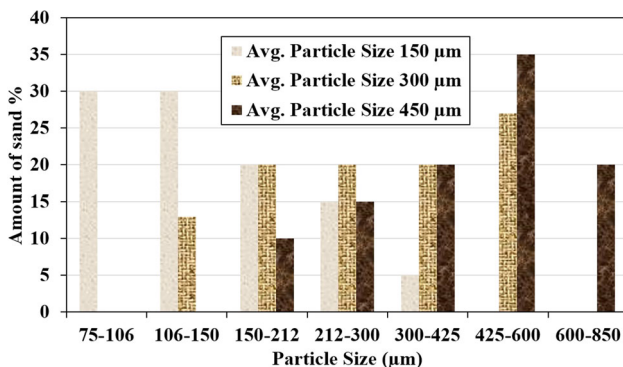


Fig. 3 Particle size distribution of sand samples having average particle size of 150, 300, and 450 μm

Qualitech Systems, India. The thickness of coatings was measured using a metallurgical image analysis system (QSMIAS-4.0). Further, their surface morphology after erosion was also investigated using EDS and SEM micrographs obtained from SEM JEOL, JSM-6510LV. A surface roughness tester (SURTRONIC SE 1200, Taylor Hobson) was used to measure the surface roughness of coated as well as uncoated samples before and after erosion. A digital micro-Vickers hardness tester (HVD-1000LCD by Qualitech Systems, India) was used to measure the microhardness of the coatings and steel. A load of 1000 g was applied for a dwell time of 20 s, and the average of fifteen microhardness readings was taken in each case.

Contact Angle Measurement

A contact angle analyzer (Goniometer: First Ten Angstrom) was used to measure the contact angle (CA) for SS 316, coating A, and coating B samples before and after erosion. The standalone samples were polished using 400 grit size paper before the measurement (Ref 46). The samples were processed using ethanol, followed by cleaning using compressed air before the measurement. The volume of the water drop was measured to be 9 μl . Generally, it was seen that the drop would get stable after 0.8 s (Ref 46). So, in the present study, the contact angle measurement was done after 1.5 s when the drop touched the surface. For the said surfaces, CA measurement was a challenge because of the obstructions imposed by projections in front of drops. Due to these obstructions, the point of contact of the drop and surface was not clear, and it misleads to a lesser CA measurement. Further, the point of contact was located by following the curvature of the drop with complete caution. CA angle measurement was done using ImageJ software.

Slurry Erosion Test Rig

Slurry erosion testing of the said samples was carried out using Water (Slurry) Jet Erosion Test Rig (TR411 by Ducom, India). A schematic diagram of the test rig used is shown in Fig. 5. Impingement of the slurry is executed on the stationary sample in a similar manner as done by Grewal et al. (Ref 2). The test rig consists of a sand/erodent hopper (60 kg capacity), which is being filled with the sand having predetermined average particle size. The water tank located at the bottom consists of a 10-mm water filter, which circulates only clear water. Every time, new erodent particles are used. The clear water is pumped by a positive displacement rotary vane pump powered by 1.5 kW 3-phase AC motor to the mixing chamber at high pressure. By changing the rpm of said motor, the amount of water

Fig. 4 SEM micrographs and EDS analysis of sand particles having average particle sizes as (a) 450 μm , (b) 300 μm , and (c) 150 μm

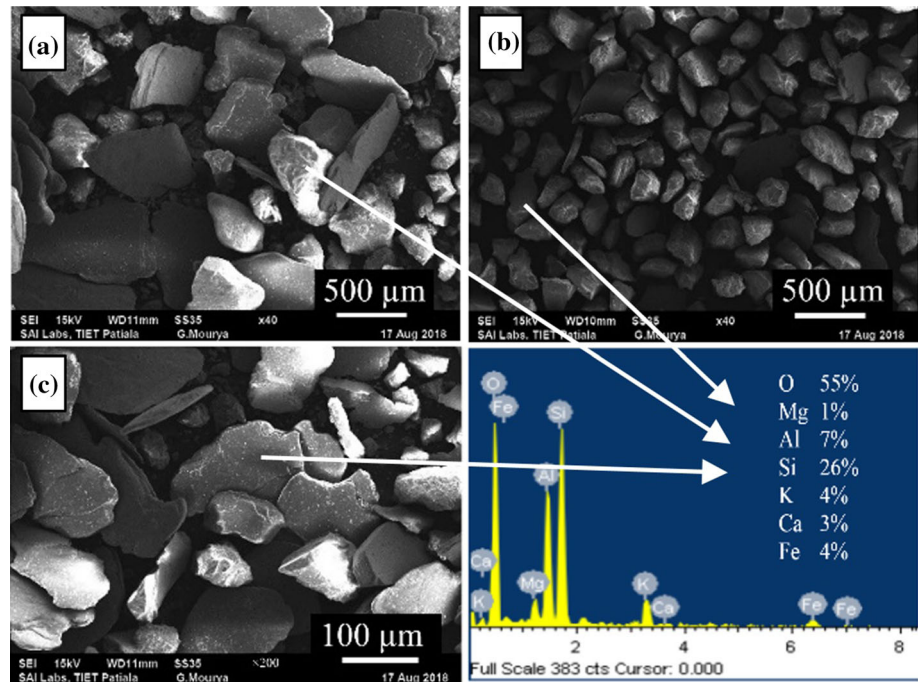
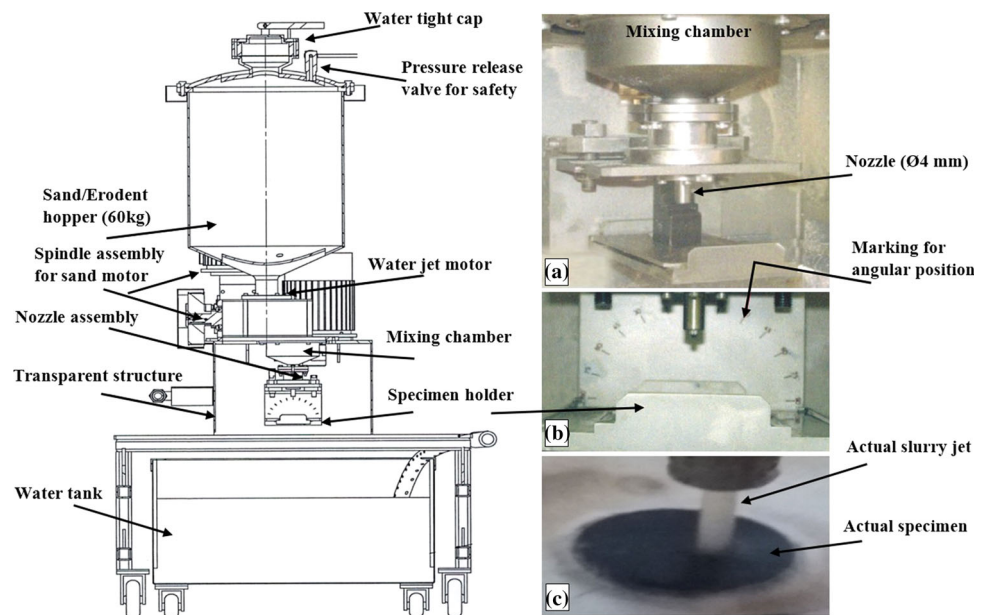


Fig. 5 Schematic diagram of Water (Slurry) Jet Erosion Test Rig (TR411, Ducom, India). Actual image of (a) nozzle and mixing chamber assembly (b) with marking sheet for angular position of specimen holder (c) jet striking the sample



pumped to the mixing chamber and its pressure can be controlled. Further, the fresh erodent particles from the hopper enter to the mixing chamber through a spiral (worm) powered by a separate 3-phase AC motor with gear reduction. The amount of erodent particles can be controlled by changing the rpm of erodent motor. The discharged fresh erodent (due to rotation of spiral worm) mixes with the high-pressure water inside the mixing chamber as shown in Fig. 5(a), this high-pressure slurry comes out from the nozzle situated at the bottom of mixing chamber and impinges on the specimen held firmly in the

specimen holder. The impingement angle can be changed by changing the orientation of the specimen holder against the marked scale as shown in Fig. 5(b). The effect of four impingement variables (impact velocity, angle of contact, concentration, and particle size) was analyzed using the slurry erosion test rig. The coated and uncoated samples were held firmly in the specimen holder to perform the slurry erosion test. The procedure given in ASTM G-73 was followed for performing the slurry erosion tests. The samples were washed with acetone and dried before and after erosion test. The weight of the exposed samples

before and after erosion was measured using electronic microbalance (Citizen CY204 by Denver Instruments GmbH, Germany) having least count of 0.1 mg. Before slurry erosion, the specific masses of SS 316, coating A, and coating B were found to be 7.8, 12.5, and 2.2 g/cc, respectively (Ref 6, 47). From the weight loss, densities and time of test, the volume erosion rate (mm³/h) was calculated.

Slurry Erosion Testing Conditions

As discussed earlier, the impingement conditions like impact velocity, angle of contact, concentration, and particle size play a major role in slurry erosion of the material (Ref 2, 8-12). So, in the present research work, the effect of these four impingement variables on slurry erosion of coated as well as uncoated samples was investigated. Three levels for each variable were selected as shown in Table 3.

Three different impact angles (90°, 60°, and 30°) were selected to analyze the type of erosion mode shown by the coated and uncoated samples. The material with ductile behavior shows highest erosion in the range of 20°-40°, whereas the material having brittle behavior shows highest erosion for 90° impact angle (Ref 48, 49). The maximum slurry concentration in submersible pump reaches up to 45,000 ppm during the initial hours and decreases as the time passes. So, in the present study, three concentrations (15,000, 30,000, and 45,000 ppm) were selected for analysis. For achieving concentration as 45,000 ppm, 45 gm of predetermined sand was mixed in 1 liter of water. In order to analyze the influence of the impingement variables on slurry erosion using Taguchi approach, L₉ orthogonal array was used for conducting the experiments; the same is shown in Table 4.

The slurry erosion of the coated, as well as, uncoated samples for the above-said experimental combinations was carried out for an hour in each case. The nozzle diameter and standoff distance were kept constant as 4 mm and 2.5 cm, respectively, during the slurry erosion test. After slurry erosion, it was found that the volume loss per unit time in each case was maximum for Run-7. Afterward, the effect of angles was analyzed by performing the slurry erosion for Run-10 and Run-11 as mentioned in Table 5, keeping the other parameters as constant with regard to Run-7. Further, the slurry erosion of samples for a single

parametric combination (Run-7) was also investigated for extended hours.

Results and Discussion

Metallurgical and Mechanical Characterization of the Coatings

Cross-sectional micrographs of coating B are shown in Fig. 6. Some microvoids are observed in the HVOF-sprayed coating part, which contributes to the porosity. The interface between the coating A and SS 316 is observed to be defect-free as shown in Fig. 6(b). The HVOF-sprayed part is found to have a nearly uniform thickness with a mean value of 302 μm; Fig. 6(c). The thickness of PTFE coating was controlled by the amount of powder sprayed. In a pilot study, it was observed that the erosion rate decreases with decrease in the thickness of PTFE coating with a threshold level of 62 μm. So, the average thickness of PTFE coating was maintained as 62 μm as shown in Fig. 6(d).

Moreover, inclusion of PTFE in the uppermost portion of HVOF coating was seen at the interface of coating A and coating B; Fig. 6(d). This indicates that the polymer showed a tendency to make a strong adhesive bonding with the HVOF-sprayed coating by seeping-in the upper layers of the latter.

Table 4 Experimental runs as per the L₉ orthogonal array

Experiment no.	Levels of parameter			
	ppm	μm	m/s	Degree
Run-1	1	1	1	1
Run-2	1	2	2	2
Run-3	1	3	3	3
Run-4	2	1	2	3
Run-5	2	2	3	1
Run-6	2	3	1	2
Run-7	3	1	3	2
Run-8	3	2	1	3
Run-9	3	3	2	1

Table 3 Parameters along with their range and levels

Parameter	Concentration, ppm	Average particle size, μm	Impact velocity, m/s	Impact angle, °
Level-1	15,000	150	15	90
Level-2	30,000	300	25	60
Level-3	45,000	450	35	30

The average thickness, apparent porosity, average surface roughness (Ra), and microhardness values of investigated specimens are given in Table 6. The microhardness of the steel (SS 316) varies from 255 HV_{9,81N} to 290 HV_{9,81N}, with an average value of 273.60 HV_{9,81N}. After the application of coating A, the average hardness of the steel got increased to 922.20 HV_{9,81N}, maximum and minimum values as 958 HV_{9,81N} to 882 HV_{9,81N},

respectively. This variation in microhardness is expected due to the presence of various features present in the coating microstructure, such as voids, oxides, splats, and splat boundaries, which make the coating anisotropic in nature, whereas the top PTFE coating exhibited a very low average microhardness as 11.50 HV_{9,81N} due to its soft nature. Further, zero porosity was seen in case of coating B that may be due to the uniform melting of PTFE during sintering. The average apparent porosity of coating A was found to be 1.57% which falls in the porosity range of 1.4–2% reported in literature for similar HVOF-sprayed coatings (Ref 6, 50). The average roughness (Ra) value of coating A was reported to be 2.868 μm , which is approximately four times the average roughness (Ra) value of SS 316. However, when a topcoat of PTFE was deposited on HVOF coating, the average roughness (Ra) value decreased to 1.514 μm .

Table 5 Parametric combinations for analyzing the effect of impact angles

Experiment no.	Levels of parameter			
	Ppm	μm	m/s	Degree
Run-7	45,000	150	35	60
Run-10	45,000	150	35	30
Run-11	45,000	150	35	90

Fig. 6 Cross-sectional micrographs representing (a) both WC-10Co-4Cr and PTFE coatings (coating A and B), (b) intersection of HVOF-sprayed coating (coating A) and bare steel (SS 316), (c) HVOF-sprayed coating (coating A) thickness, and (d) PTFE coating (coating B) thickness

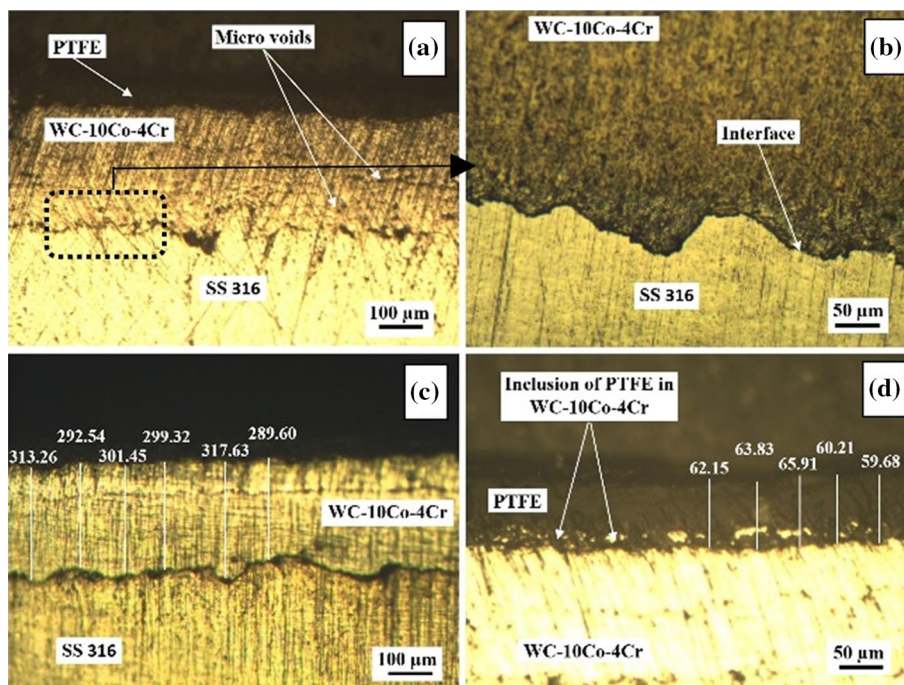


Table 6 Thickness, apparent porosity, average surface roughness (Ra), and microhardness of different specimens

Material/coating	Thickness, μm	Porosity, %	Roughness (Ra), μm	Average microhardness (HV _{9,81N})
Bare steel (SS 316)	0.740	274
HVOF-sprayed WC-10Co-4Cr coating (coating A)	302	1.57	2.868	922
PTFE-modified HVOF-sprayed WC-10Co-4Cr coating (coating B)	62	0	1.514	12

Contact Angle Analysis

Contact angle (CA) measurement for the coated as well as, uncoated samples, was carried out as discussed earlier. CAs for coating B, coating A, and SS 316 samples before and after erosion are compared as shown in Fig. 7. Coating B exhibits superhydrophobic nature as the CA for the same was found to be 152° (Ref 51). A slight decrement of approximately 4° was observed in CA for the coating B sample after exposure to the slurry erosion conditions of Run-7 for an hour, which may be due to the decrease in surface roughness of the sample. However, the above material still exhibits hydrophobic behavior even after the slurry erosion, which is in accordance with the results obtained by Chen et al. (Ref 40) who concluded that the coatings with multiple length-scale structures having PTFE as topcoat retain the superhydrophobicity even after severe mechanical abrasion.

The coating A has higher value of CA as compared to the SS 316. It may be due to the presence of more protrusions as concluded from the higher surface roughness of coating A as compared to the SS 316. Moreover, from the drop image of coating A, the material seems to exhibit Wenzel state (Ref 37). The coating B exhibits more value of CA as compared to the coating A even though the surface roughness of the latter is more. This may be attributed to the hydrophobic nature of the PTFE. Due to the hydrophobic nature of PTFE, the drop on the coating B seems to exhibit Cassie-Baxter state (Ref 37, 52). After slurry erosion, the CA value for SS 316 increases slightly; however, the CA value for the coating A decreases by 9–10°. This may be due to increase and decrease in surface roughness values of the SS 316 and coating A, respectively, after slurry erosion.

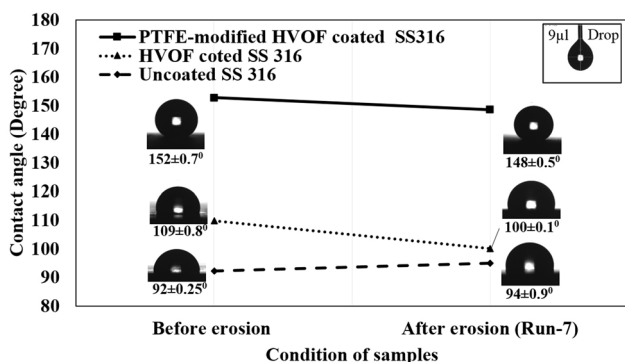


Fig. 7 Contact angle (CA) for PTFE-modified HVOF-sprayed WC-10Co-4Cr coated (coating B), standalone HVOF-sprayed WC-10Co-4Cr coated (coating A), and bare steel (SS 316) samples before and after erosion subjected to Run-7 (highest impact velocity: 35 m/s, impact angle: 60°, maximum concentration: 45,000 ppm and minimum average particle size: 150 μm)

Slurry Erosion Analysis

To evaluate the effect of coating A and coating B on slurry erosion of the steel, the coated and uncoated specimens were subjected to slurry erosion conditions as discussed earlier. Figure 8 represents the bar-chart comparison of volumetric erosion rates for the investigated samples for all the nine experimental runs; designed on the basis of L₉ orthogonal array as discussed earlier. The erosion in each case was found to be maximum for the Run-7 (highest impact velocity: 35 m/s, impact angle: 60°, maximum concentration: 45,000 ppm and minimum average particle size: 150 μm). It was also observed that coating A has lesser erosion wear rates as compared to SS 316 during each run. This may be attributed to the higher hardness of the coating A as compared to the bare material (SS 316).

Moreover, an improvement in the slurry erosion resistance was noticed when a topcoat of PTFE was applied on the standalone coating A, even though the coating B has a negligible hardness as compared to the standalone coating A and uncoated SS 316. This may be attributed to the superhydrophobic nature of the coating B as the CA value for the same was observed to be approximately 150°. Due to superhydrophobic nature, the material repels the water in the opposite direction, and a very few erodent particles are impacting on the target surface with full flow, while others lose their kinetic energy when encountering the water particles moving in the opposite direction.

Furthermore, Taguchi linear model analysis was used to see the effect of different parameters on the slurry erosion of various samples (Ref 53). The signal-to-noise ratios for coating A, coating B, and SS 316 samples were calculated assuming response variable (erosion wear) as smaller the better. The mean data plots of S/N ratio are shown in Fig. 9(a), (b), and (c).

From the results, it was concluded that the minimum erosion wear should occur for the parametric combinations;

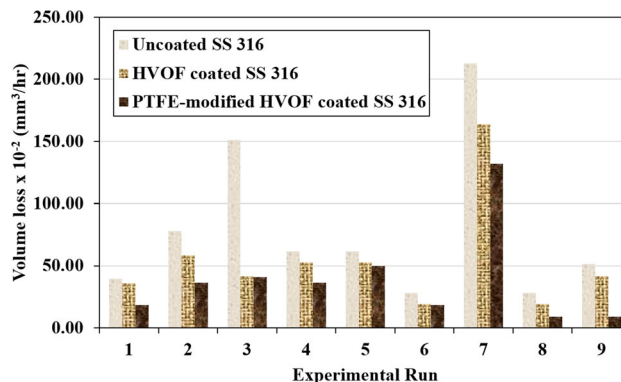


Fig. 8 Volumetric erosion rates for PTFE-modified HVOF-sprayed WC-10Co-4Cr coated (coating B), standalone HVOF-sprayed WC-10Co-4Cr coated (coating A), and uncoated (SS 316) steels

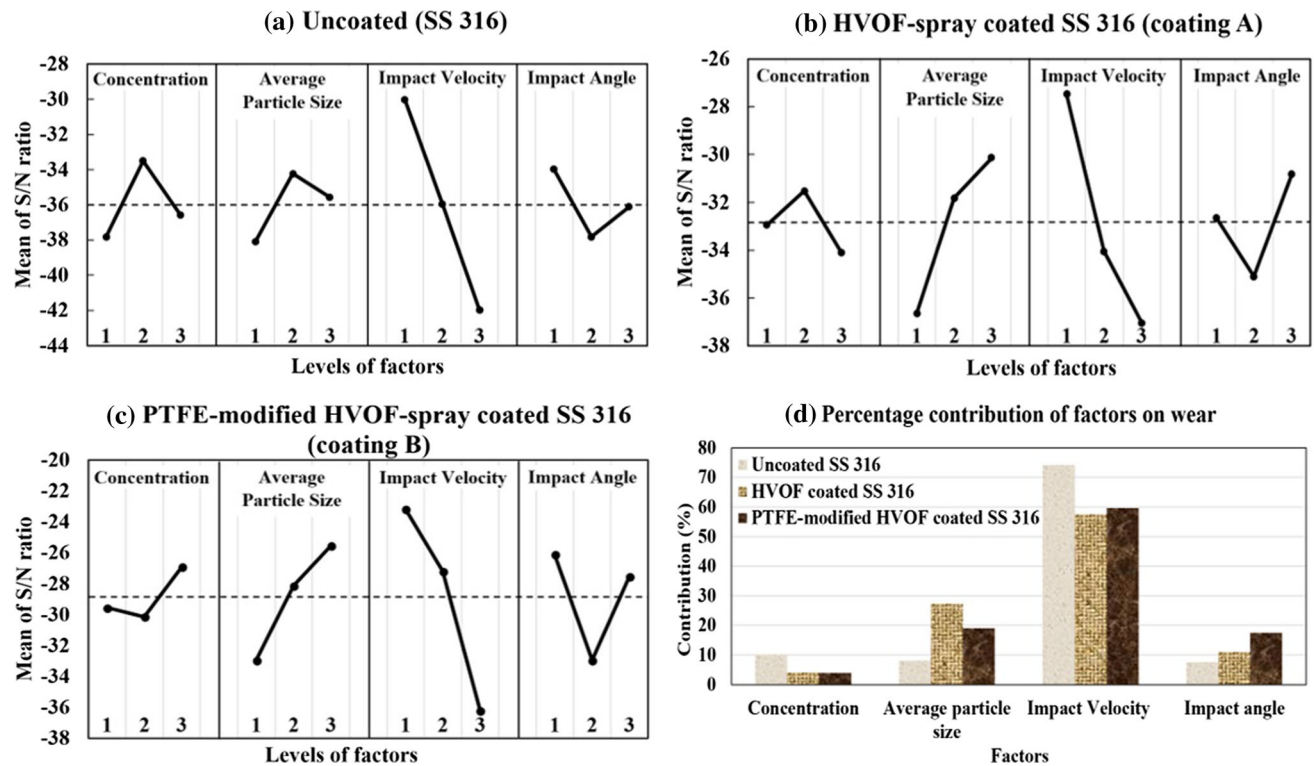


Fig. 9 S/N ratio for (a) Uncoated (SS 316) (b) HVOF-sprayed coated SS 316 (coating A) (c) PTFE-modified HVOF-sprayed coated SS 316 (coating B) (d) % contribution of various factors to slurry erosion wear

(2-2-1-1), (2-3-1-3), and (3-3-1-1) for SS 316, coating A, and coating B samples, respectively. But, none of these combinations are covered in the designed L_9 orthogonal array. Further, the validation of these parametric combinations was done by conducting the experiments again for said samples subjected to these identified combinations. Based upon these experiments, the volumetric erosion rates for SS 316, coating A, and coating B samples under the parametric combinations (2-2-1-1), (2-3-1-3), and (3-3-1-1) were found to be 20.51×10^{-2} , 16×10^{-2} , and 4.55×10^{-2} , respectively, which come out to be minimum among the volumetric erosion rates observed for various parametric combinations of L_9 orthogonal array. So, the results obtained are in accordance with the Taguchi results. Based upon these data, it may be recommended to use the identified parametric combinations (2-2-1-1), (2-3-1-3), and (3-3-1-1) for SS 316, coating A, and coating B materials, respectively, during the operation of hydro-machineries, although this may not be always possible to run the turbines due to other constraints. From the mean data plot of S/N ratio, it was concluded that the maximum slurry erosion should occur for the parametric combinations; (1-1-3-2), (3-1-3-2), and (2-1-3-2) for SS 316, coating A, and coating B samples, respectively. Therefore, it can be recommended to avoid these parametric combinations during the operation of hydro-machineries. It was also observed

from Taguchi results that the maximum erosion occurs for the parametric combinations consist of minimum average particle size, maximum impact velocity, and 60° impact angles for all the samples. The combination of these three parameters was also covered in Run-7, which contributes to maximum erosion among all the 9 runs of L_9 orthogonal array. Hence, it may be concluded that the erosion wear increases with the decrease in average particle size and increase in impact velocity. It is perceived that number of particles per unit area (flux) striking the surface are more in case of lowest average particle size of $150 \mu\text{m}$ as compared to average particle size of $450 \mu\text{m}$ that might have contributed to more erosion in case of smaller average particle size. Secondly, kinetic energy is proportional to the square of velocity. Therefore, with increase in velocity, kinetic energy of the particles also increases even for the smaller sand particles; this may be the possible reason behind the increase in erosion rate with increase in velocity and decrease in average particle size. The trend of increase in erosion wear with increase in impact velocity comes in accordance with the results obtained by Elkholy et al. (Ref 54) and Goyal et al. (Ref 6).

Further, analysis of variance for S/N ratio was done for calculating the percentage contribution of various factors on the slurry erosion of the given samples (Ref 53). The percentage contribution of factors on the slurry erosion of

various samples was compared using a bar graph as shown in Fig. 9(d). The results show that impact velocity has maximum contribution of 74.2, 57.6, and 59.7% on slurry erosion of SS 316, coating A, and coating B samples, respectively. So, in this aspect, coating B is preferred for the hydro-machinery applications, where the impact velocity may be kept maximum. The effect of impact velocity decreases with the coating as compared to bare steel (SS 316), and approximately same contribution was seen for both coating A and coating B samples. The concentration stood second in contribution for bare SS 316, whereas the minimum effect of concentration was reported in case of coating A and coating B samples. This observation indicates that both the coatings could be recommended for the hydro-machinery components working under high slurry concentration. Further, for the coated samples, the contribution of average particle size is next to the impact velocity followed by impact angle and slurry concentration, respectively.

Afterward, the effect of angles was analyzed by performing the slurry erosion experiment on the coated as well as uncoated samples for the parametric combinations as mentioned in Table 5. During these tests, the other parameters comprising concentration: 45,000 ppm, average particle size: 150 μm and impact velocity: 35 m/s were kept constant. The results obtained are represented in Fig. 10. It was observed that the volumetric slurry erosion was found to be maximum for an impact angle of 60° followed by 90° and 30° for all the investigated materials. It means the materials show mixed behavior of brittleness as well as ductility (Ref 48, 49). Further, all the three materials exhibit better erosion resistance against 30° impact angle. The coating A showed a better erosion resistance as compared to the bare SS 316 steel, which is due to its higher microhardness as compared to the bare material. Further, improvement in the erosion resistance was observed for the coating A when a topcoat of PTFE

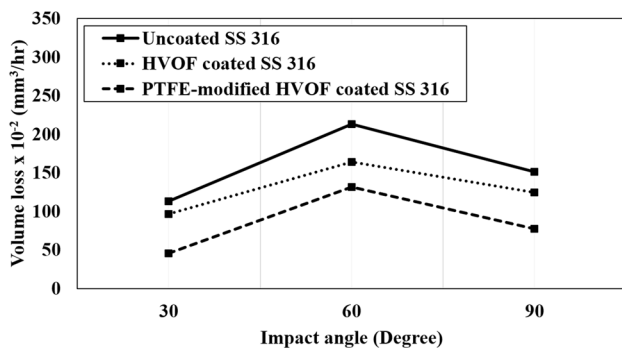


Fig. 10 Volumetric erosion rates for PTFE-modified HVOF-sprayed WC-10Co-4Cr coated (coating B), standalone HVOF-sprayed WC-10Co-4Cr coated (coating A), and uncoated (SS 316) steels v/s impact angles as mentioned in Table 5

was applied, which may be due to the superhydrophobic nature of the PTFE coating as observed from the CA measurement.

From the above results, the volumetric slurry erosion was found to be maximum for the Run-7 (highest impact velocity: 35 m/s, impact angle: 60°, maximum concentration: 45,000 ppm and minimum average particle size: 150 μm) for all the materials. Therefore, the slurry erosion of the coated as well as the uncoated samples for this parametric combination (Run-7) was also investigated for an extended duration. The cumulative volumetric erosion data for the coating B and coating A along with that for the SS 316 steel are shown in Fig. 11.

From the erosion testing results for the extended hours, it was observed that the coating A showed comparatively higher erosion resistance in comparison with SS 316. Further improvement in the erosion resistance was observed when the topcoat of PTFE was applied to it. The results obtained for extended hours are in accordance with the results obtained initially for all the sets of parameters under L₉ orthogonal array. It may be concluded that both the coatings are stronger as well as durable as compared to the bare material, when subjected to the erosion conditions. Moreover, it is evident that the volumetric erosion rate of coated as well as uncoated specimens was comparatively higher during the initial hours. In case of coating B and coating A, it may be due to the presence of initial micro-peaks and valleys in the coatings, which decrease with the erosion. Further, in some cases, abrupt change was seen that might attribute to the spallation of material from the surface during the erosion. It was also observed that the volume loss for coating B became approximately negligible in the fifteenth hour. For the coating A, the volume loss is more than the coating B, but lesser than the base material

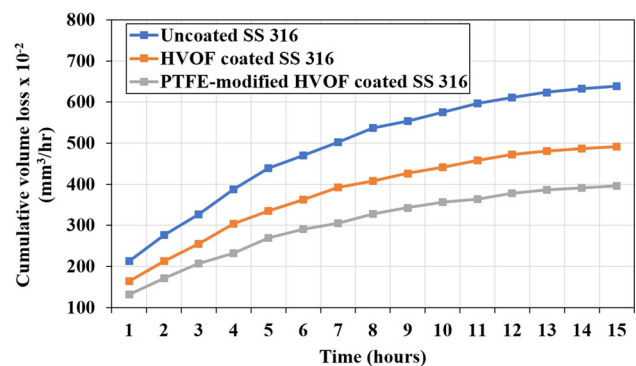


Fig. 11 Influence of time on cumulative volumetric erosion rate of PTFE-modified HVOF-sprayed WC-10Co-4Cr coated (coating B), standalone HVOF-sprayed WC-10Co-4Cr coated (coating A) and uncoated (SS 316) steels subjected to parametric combination of Run-7 (highest impact velocity: 35 m/s, impact angle: 60°, maximum concentration: 45,000 ppm and minimum average particle size: 150 μm)

SS 316. However, steady and continuous volume loss was observed for the bare SS 316.

Analysis of Erodent Surfaces

The mechanisms behind the material removal by slurry erosion mainly depend upon the properties of erodent as well as targeted surfaces (Ref 6, 55). Further, it was also reported that the material exhibits different erosion mechanisms depending upon its ductile and brittle behavior. For ductile materials, mechanism of erosion is dictated mainly by direct micro-plowing and micro-cutting of the plastically deformed areas of the exposed surfaces, whereas, in case of brittle materials, erosion takes place by the fatigue failure of the exposed surfaces owing to the repeated impacts of slurry (Ref 6, 56). Further, despite the properties of material and erodent particles, the erosion mechanism also depends upon the impingement conditions during the slurry erosion (Ref 57). An attempt has been made in the current study to analyze the possible mechanisms behind the erosion; therefore, SEM analysis of the eroded specimens was done. The SEM images of erodent portions were taken for the samples exposed to the slurry erosion under parametric combination mentioned in Run-7 and Run-8 for 1 h, which contributes to the maximum and minimum erosion, respectively. The used erodent (sand) particles were also examined using SEM micrographs. The EDS analysis of the above-said eroded surfaces was also carried out to see the imbedded elements, if any.

Bare Steel (SS 316)

A SEM image of bare SS 316 is shown in Fig. 12. The surface is found to have some polishing and cutting marks.

SEM images for different eroded portions of uncoated SS 316 subjected to slurry erosion conditions of Run-7

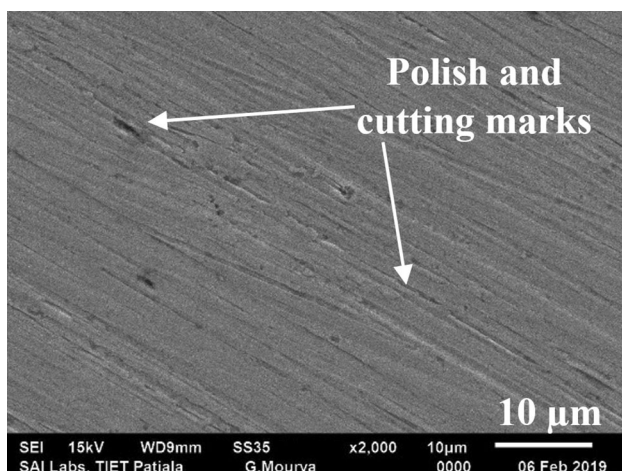


Fig. 12 SEM image of uncoated steel (SS 316) before slurry erosion

(impact velocity: 35 m/s, impact angle: 60°, concentration: 45,000 ppm and average particle size: 150 μm) for 1 h along with the EDS graph are shown in Fig. 13. The possible typical erosion signatures as seen from the SEM images are also represented in Fig. 13. The lip formation (micro-plowing) was observed very frequently in SS 316, which may be due to the plastic deformation of the material under impact of erodent particles. The removal and fracture of these lips was also observed. These mechanistic observations are in good agreement with the mechanisms reported by Manisekaran et al. (Ref 58) for slurry erosion of the 13Cr-4Ni steels. Moreover, the material from the surface may be removed due to the presence of a greater number of micropores, followed by the crater formation as seen on the eroded surfaces, which may be due to the higher slurry concentration of 45,000 ppm. These observations are in accordance with the results observed by Santa et al. (Ref 17) and Goyal et al. (Ref 6) for the slurry erosion of the ASTM743 CA6NM steel and CF8 M steel, respectively. A very few micro-cutting features were also observed in the form of wear marks on the eroded surfaces. The presence of these wear marks increases with a decrease in the angle of impingement; however, in case of Run-7, the angle of impingement is 60°, which may be the reason behind the lesser number of wear marks in the form of micro-cutting. From the EDS analysis, it was observed that O, Si, and Al elements are also present in the eroded portions along with the other constituents of the material itself, which signify the embedment of erodent particles in the material. The above embedment may be due to the higher kinetic energy of the erodent particles under the maximum impact velocity of 35 m/s and the softer nature of SS 316 as compared to the erodent particles. Furthermore, due to more and more impacts of the slurry with the passage of time, the embedded particles may further be removed by producing a leftover cavity termed as micropores as seen in the SEM images of Fig. 13.

SEM images for eroded portion of uncoated SS 316 subjected to slurry erosion conditions of Run-8 (impact velocity: 15 m/s, impact angle: 30°, concentration: 45,000 ppm and average particle size: 300 μm) for 1 h along with the EDS graph are shown in Fig. 14. The possible erosion signatures as observed from SEM image are also represented in Fig. 14. The plowing and wear marks were observed very frequently even though the velocity is minimum as 15 m/s for Run-8, which may be due to the lower impact angle of 30°. Further, like Run-7, micropores and craters were also visible on the eroded surface subjected to Run-8, which may be due to higher concentration of 45,000 ppm. Furthermore, embedment of eroded particles was also concluded from the presence of O, Si, and Al elements as observed from the EDS graph. The absence of lip formation and their fracture sites on the eroded surface

Fig. 13 (a), (b), and (c) SEM images and (d) EDS plot of eroded portions of bare steel (SS 316) exposed to slurry conditions of Run-7 (impact velocity: 35 m/s, impact angle: 60°, concentration: 45,000 ppm and average particle size: 150 μm) for 1 h

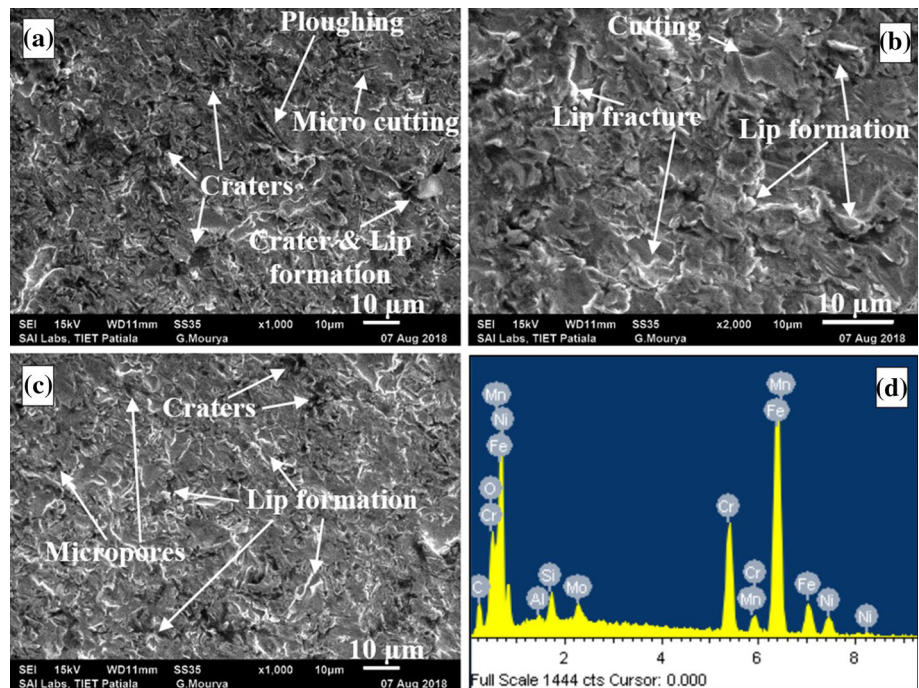
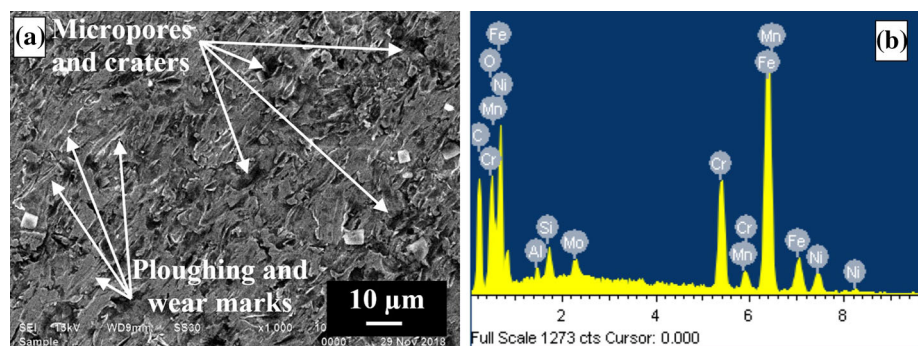


Fig. 14 (a) SEM image and (b) EDS plot of eroded portion of bare steel (SS 316) exposed to slurry conditions of Run-8 (impact velocity: 15 m/s, impact angle: 30°, concentration: 45,000 ppm and average particle size: 300 μm) for 1 h



may be the probable reason behind the lower slurry erosion of SS 316 subjected to Run-8.

HVOF-Sprayed WC-10Co-4Cr Coated SS 316 Steel (Coating A)

A SEM image for coating A is shown in Fig. 15. It was seen from the image that the interlocked splats with some unmelted fine particles are uniformly distributed on the surface. In the image, dark or gray portion represents Co-Cr binder phase and bright portion may be due to the decarburization in the WC region; similar results were also observed previously for WC-Co-based coatings (Ref 6, 59, 60). Further, some microvoids are also seen in the coating microstructure reported in the image.

SEM/EDS analysis of different eroded portions of coating A subjected to slurry erosion condition of Run-7 for 1 h is shown in Fig. 16. The possible typical erosion signatures as seen from the SEM images are also

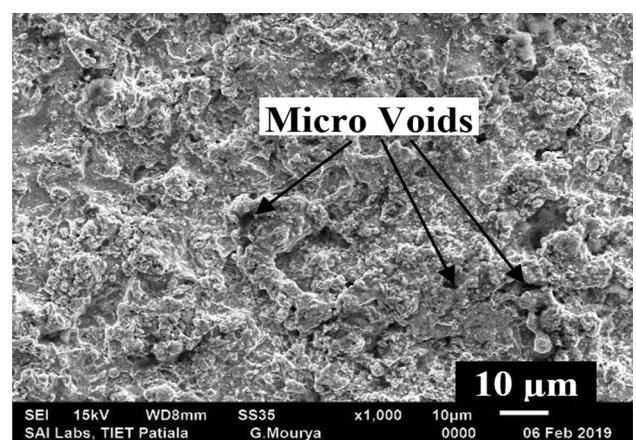


Fig. 15 SEM image of HVOF-sprayed WC-10Co-4Cr coated SS 316 (coating A) before slurry erosion

highlighted in Fig. 16. From the SEM images, it was observed that the chipping of material is a very common mechanism for the coating A; which may be due to the

removal of loosely bonded WC grains from the surface, which were seen as brighter portion in the uneroded HVOF coating as shown in Fig. 15. This observed aspect is in accordance with the results reported by Ninham et al. (Ref 61). Further, wear or cutting marks are also reported on the surface, which may be the starting phase for the removal of an upper layer of binder material followed by the removal of loosely bounded WC particles from the surface. Similar observations are reported in the literature (Ref 6, 62–64). The material shows negligible signatures of plastic deformation and lip formation, contrary to the bare material (SS 316), leading to lesser erosion in the former case. Moreover, some deeper and darker craters are also seen on the surface of the eroded coating, which were also observed by Thakur et al. (Ref 64). The formation of such features takes place by the repetitive impact of high-speed erodent particles causing the removal of WC particles leaving behind craters. The coating, in general, exhibited a ductile mode of erosion which is perceptible from the fact that there are no cracks on the eroded surfaces as could be seen from the SEM images. This observation is in good agreement with the reported literature (Ref 6, 61–64). From the EDS graph, it is seen that no element other than the basic constituents of the material and coating is reported in the eroded portion of the coating, which implies the absence of embedment of erodent particles in the coating after erosion, which is desirable attribute. This may be due to hard nature of HVOF coating.

SEM/EDS analysis along with the possible erosion signatures of eroded portion of coating A subjected to

slurry erosion condition of Run-8 (impact velocity: 15 m/s, impact angle: 30°, concentration: 45,000 ppm and average particle size: 300 μm) for 1 h is shown in Fig. 17. As seen from the SEM images, wear or cutting marks are visible on the eroded surface, which may be due to the lower impact angle of 30° in case of Run-8. Further, these marks may be considered as the starting phase pertaining to removal of an upper layer of binder material. Moreover, some deeper and darker craters are also seen on the surface, like the observation made in case of eroded surface subjected to impingement condition of Run-7. The absence of traces related to chipping of material on the eroded surface may be the possible reason behind lower erosion rate of coating A subjected to Run-8. From the EDS graph, the absence of O, Si, and Al elements implies the absence of embedment of erodent particles in the surface of coating A after erosion, which may be due to the harder nature of HVOF coating.

PTFE-Modified HVOF-Sprayed WC-10Co-4Cr Coated SS 316 Steel (Coating B)

A SEM image of the uneroded coating B is shown in Fig. 18, which indicates that the PTFE is uniformly spread over the HVOF coated material with the presence of a negligible concentration of voids.

SEM/EDS analysis of eroded coating B subjected to slurry erosion condition of Run-7 for 1 h is shown in Fig. 19. As seen from the SEM images, only a very few wear marks or spots are visible on the eroded surface,

Fig. 16 (a), (b), and (c) SEM images and (d) EDS plot of eroded portions of HVOF-sprayed WC-10Co-4Cr coated SS 316 (coating A) exposed to slurry conditions of Run-7 (impact velocity: 35 m/s, impact angle: 60°, concentration: 45,000 ppm and average particle size: 150 μm) for 1 h

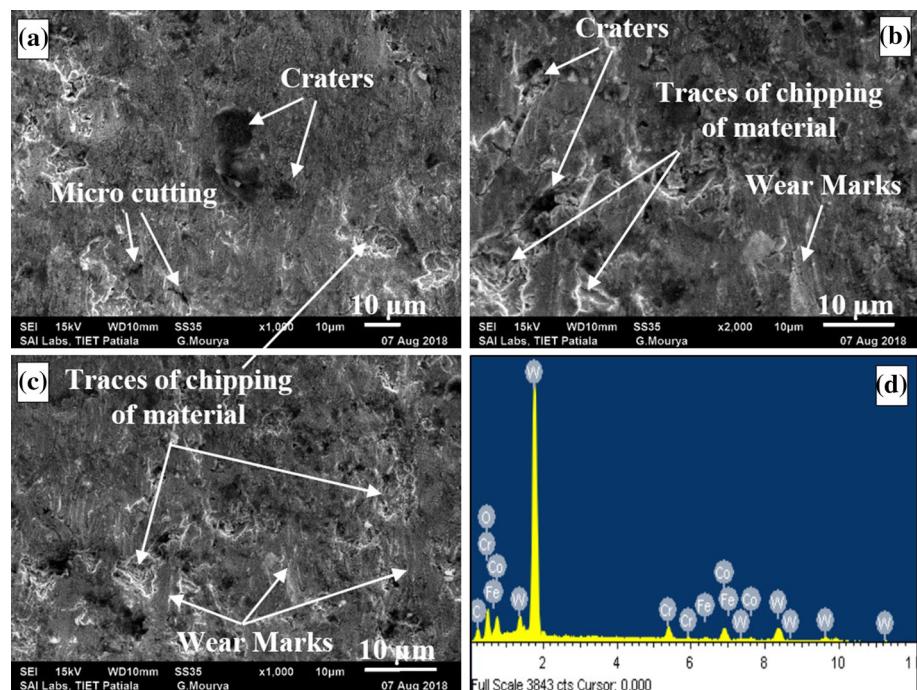


Fig. 17 (a) SEM image and (b) EDS plot of eroded portion of HVOF-sprayed WC-10Co-4Cr coated SS 316 (coating A) exposed to slurry conditions of Run-8 (impact velocity: 15 m/s, impact angle: 30°, concentration: 45,000 ppm and average particle size: 300 μm) for 1 h

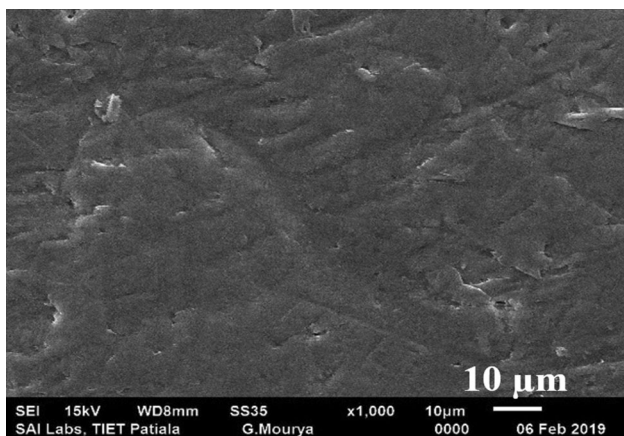
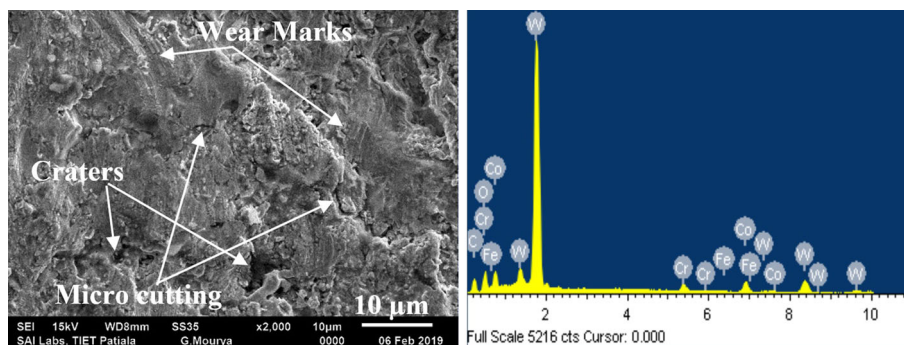


Fig. 18 SEM image of PTFE-modified HVOF-sprayed WC-10Co-4Cr coated SS 316 (coating B) before slurry erosion

indicating relatively lower magnitude of erosion. The surface shows a superhydrophobic nature as concluded from the CA values obtained for the coating, which means the material repels the water striking on it and tries to formulate the drop into an almost spherical shape. In that aspect, the erodent particles approaching toward the material feel retarded due to the repulsion of water, hence decreasing the kinetic energy of erodent particles, which in turn may be responsible for lesser erosion of the coating. Further, a very few sign of micro-plowing, craters, and microchipping of the material are visible at high resolutions, which may be due to the repetitive impact of the retarded erodent particles on the surface. Such impacts might have led to the decrease in surface roughness and CA of the surface after erosion, as has also been reported in literature (Ref 37, 40, 41). Despite the fact that the coating B has the minimum microhardness, the coating shows a minimum erosion among the investigated cases, which could be attributed mainly to the superhydrophobic nature of the PTFE coating. From the EDS analysis, it was observed that only C and F are present in the eroded portion of the surface, which means that the erodent particles are not able to embed into the coating B. This may be due to the decrease

in kinetic energy of erodent particles, retarded under the action of superhydrophobic behavior of PTFE coating.

SEM/EDS analysis of eroded portion of coating B subjected to slurry erosion condition of Run-8 (impact velocity: 15 m/s, impact angle: 300, concentration: 45,000 ppm and average particle size: 300 μm) for 1 h is shown in Fig. 20. The possible typical erosion signatures as seen from the SEM images are also highlighted in Fig. 20. On the SEM images, very few sign of craters and microchipping of the material are visible at high resolutions, which may be due to the repetitive impact of the retarded erodent particles on the surface. Further, traces of micro-plowing and lip formation along with its fracture are absent on the eroded surface of coating B subjected to impingement condition of Run-8, which may be due lower velocity for Run-8 and hydrophobic nature of the coating B. This may be the reason behind the lesser erosion of coating B subjected to impingement condition of Run-8. Furthermore, from the EDS graph, it is seen that no element other than the basic constituents of the material and coating is reported in the eroded portion of the coating B, which implies the absence of embedment of erodent particles in the coating after erosion, which is desirable attribute.

Used Erodent Sand Particles

SEM analysis of the erodent sand particles having an average size of 150 μm used for slurry erosion under a parametric combination of Run-7 for 1 h of SS 316, coating A, and coating B is shown in Fig. 21(a), (b), and (c), respectively. From the SEM image of used erodent for uncoated SS 316, it can be concluded that the edges of most of the particles get chipped out, which may be due to the impact of erodent particles with the surface or with the adjacent particles during slurry erosion. Further, the smaller particles with sharp edges may get imbedded into the surface, which may be chipped out during the repetitive impact of erodent particles causing the chipping of edges from the erodent particles and producing the crater as seen from the SEM images of erodent portion of uncoated SS

Fig. 19 (a), (b), and (c) SEM images and (d) EDS plot of eroded portions of PTFE-modified HVOF-sprayed WC-10Co-4Cr coated SS 316 (coating B) exposed to slurry conditions of Run-7 (impact velocity: 35 m/s, impact angle: 60°, concentration: 45,000 ppm and average particle size: 150 μm) for 1 h

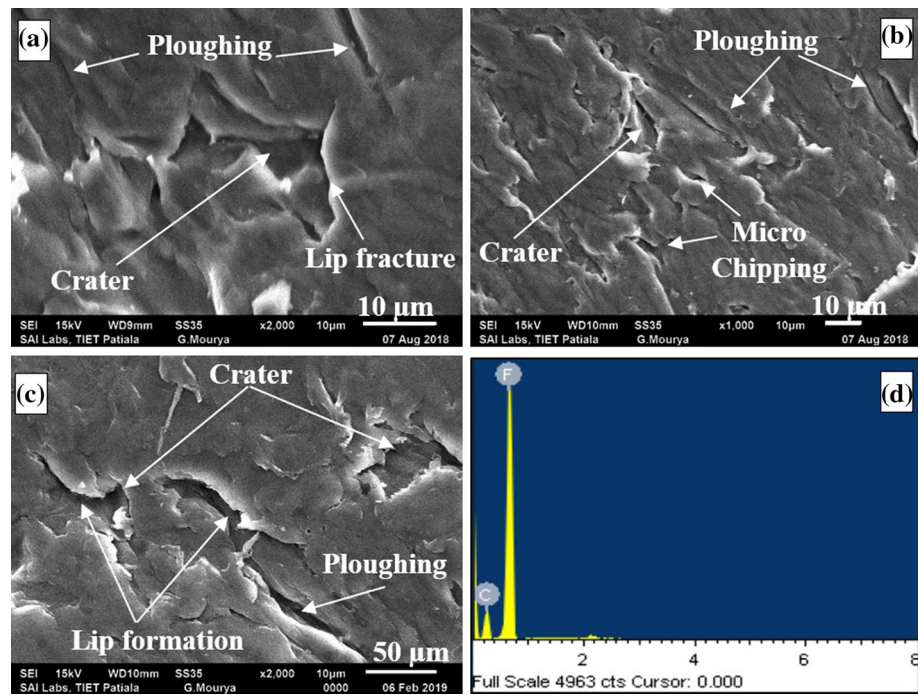
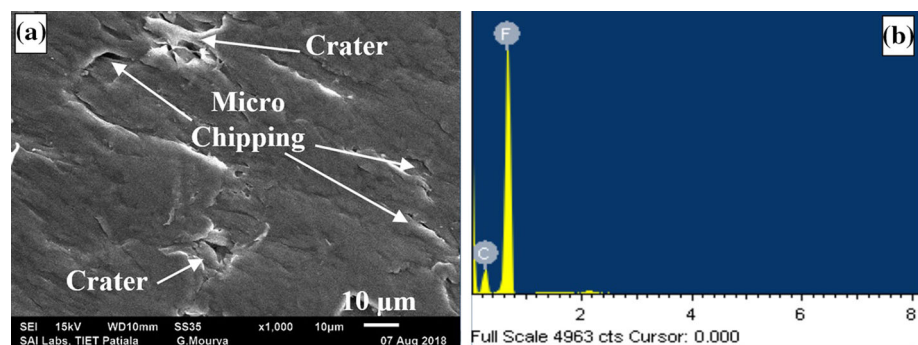


Fig. 20 (a) SEM image and (b) EDS plot of eroded portion of PTFE-modified HVOF-sprayed WC-10Co-4Cr coated SS 316 (coating B) exposed to slurry conditions of Run-8 (impact velocity: 15 m/s, impact angle: 30°, concentration: 45,000 ppm and average particle size: 300 μm) for 1 h



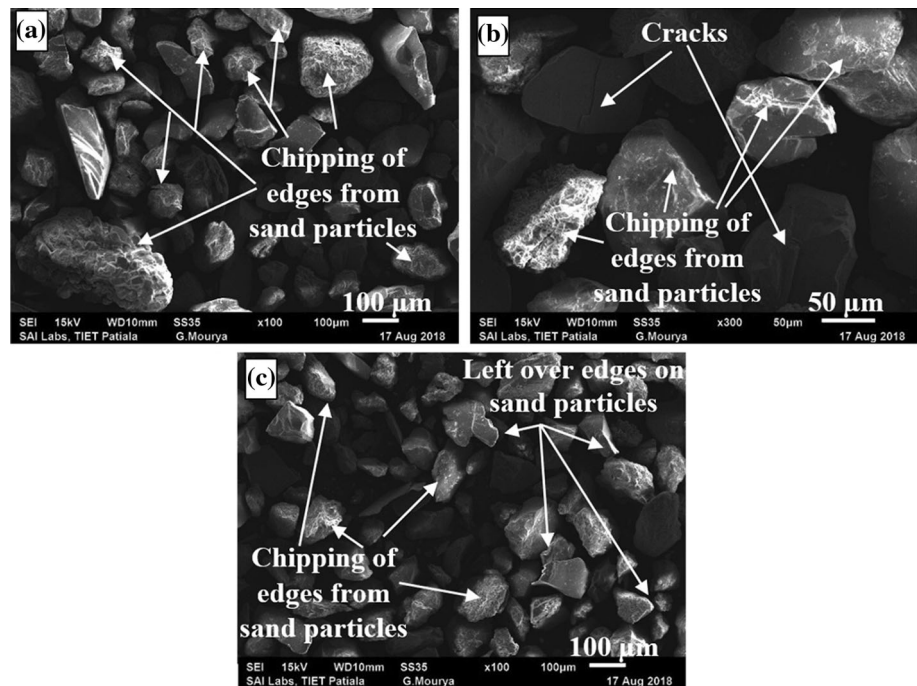
316. Moreover, some of the embedded particles may be left behind in the eroded surface, which contribute to the presence of Al, Si and O elements as reported in the EDS graph of Fig. 13(d). In the case of sand used for coating A, it can be seen that the used sand has particles with the cracks, whereas some other erodent particles have chipped-off edges. These cracks and chipped-off edges may be due to the impact with the harder surface of HVOF coating, which is not observed in the case of sand used for bare SS 316 as well as coating B. Moreover, due to the highest hardness of the HVOF coated surface, the erodent particles are not able to embed into the surface. The erodents for coating B are found to have the sharp edges, while some others have chipped-off edges. The leftover sharp edges of erodent particles may be the indicator that all the erodent particles are not able to get in contact with the surface, which may be due to the retarding action imposed by the superhydrophobic nature of the coating B. Moreover, the major reason behind the chipped-off edges may be the

collision of erodent particles with each other during the slurry erosion.

Conclusions

- HVOF-sprayed WC-10Co-4Cr coated SS 316 steel was successfully modified by a top layer of PTFE. The modified surface was found to be hydrophobic, however, with a reduced microhardness.
- The PTFE-modified HVOF coating was found to have a better slurry erosion resistance in comparison with its standalone and bare counterparts, in spite of its minimum microhardness, which may be due to its superhydrophobic nature. Moreover, the HVOF-sprayed WC-10Co-4Cr coating was also successful in reducing the slurry erosion of SS 316 steel, which could be attributed to its higher hardness.

Fig. 21 SEM images of erodent sand particles having average size of 150 μm used for slurry erosion under parametric combination of Run-7 for 1 h of (a) Bare steel (SS 316), (b) HVOF-sprayed WC-10Co-4Cr coated SS 316 (coating A), and (c) PTFE-modified HVOF-sprayed WC-10Co-4Cr coated SS 316 (coating B)



- The PTFE-modified HVOF coating showed superhydrophobic behavior with the CA of 152° , which may be due to the combined effect of more protrusions provided by the supporting HVOF coating and the hydrophobic nature of PTFE. Further, the material could maintain its hydrophobic behavior even after the exposure to the slurry erosion conditions
- Taguchi analyses indicate that the impact velocity was found to be most dominating factor in enhancing the slurry erosion rate, which implies that the kinetic energy of the erodent particles plays a major role. Moreover, the effect of average particle size was more in case of PTFE-modified HVOF-sprayed coating and standalone HVOF-sprayed coating as compared to that in the bare SS 316. Furthermore, the erosion in each case was found to be maximum for a parametric combination of impact velocity: 35 m/s, impact angle: 60° , slurry concentration: 45,000 ppm, and average particle size: 150 μm .
- Lip formation and its fracture due to repetitive impact of erodent particles was observed to be the major erosion mechanism for bare SS 316. However, the HVOF-sprayed steel showed marginal signs of plastic deformation and lip formation, and the erosion took place by dislodgement of WC particles from the binder phase. The PTFE-modified HVOF coating showed signs of a very few wear marks or spots of microplowing, craters, and microchipping of the material on the eroded surface, indicating relatively lower magnitude of erosion.

References

1. R. Chattopadhyay, High Silt Wear of Hydroturbine Runners, *Wear*, 1993, **162–164**, p 1040–1044
2. H.S. Grewal, A. Agrawal, H. Singh, and B.A. Shollock, Slurry Erosion Performance of Ni-Al₂O₃ Based Thermal-Sprayed Coatings: Effect of Angle of Impingement, *J. Therm. Spray Technol.*, 2013, **23**(3), p 389–401
3. M. Bjardal, E. Bardal, T. Rogne, and T.G. Eggen, Erosion and Corrosion Properties of WC Coatings and Duplex Stainless Steel In Sand-Containing Synthetic Sea Water, *Wear*, 1995, **50**, p 186–187
4. J. Berget, E. Bardal, and T. Rogne, Effects of Powder Composition on Erosion, Corrosion, and Erosion–Corrosion Properties of HVOF Sprayed WC Based Coatings, *Proc. Int. Thermal Spray Conf.*, 1998, **1**, p 305
5. R. Mack, P. Drtina, and E. Lang, Numerical Prediction of Erosion on Guide Vanes and in Labyrinth Seals in Hydraulic Turbines, *Wear*, 1999, **233–235**, p 685–691
6. D.K. Goyal, H. Singh, H. Kumar, and V. Sahni, Slurry Erosion Behaviour of HVOF Sprayed WC-10Co-4Cr and Al₂O₃ + 13TiO₂ Coatings on a Turbine Steel, *Wear*, 2012, **289**, p 46–57
7. A.V. Levy and P. Chik, The Effects of Erodent Composition and Shape on the Erosion of Steel, *Wear*, 1983, **89**, p 151–162
8. D. Lopez, J.P. Congote, J.R. Canob, A. Torob, and A.P. Tschiptschin, Effect of Particle Velocity and Impact Angle on the Corrosion–Erosion of AISI. 304 and AISI. 420 Stainless Steel, *Wear*, 2005, **259**, p 118–124
9. M.A. Al-Bukhaiti, S.M. Ahmed, F.M.F. Badran, and K.M. Emarab, Effect of Impingement Angle on Slurry Erosion Behaviour and Mechanisms of 1017 Steel and High-Chromium White Cast Iron, *Wear*, 2007, **262**, p 1187–1198
10. M.M. Stack and T.M. Abd El-Badia, Some Comments on Mapping the Combined Effects of Slurry Concentration, Impact Velocity and Electrochemical Potential on the Erosion–Corrosion of WC/Co-Cr Coatings, *Wear*, 2008, **264**, p 826–837

11. R. Dasgupta, B.K. Prasad, A.K. Jha, O.P. Modi, S. Das, and A.H. Yegneswaran, Effects of Sand Concentration on Slurry Erosion of Steels, *Mater. Trans.*, 1998, **39**(12), p 1185-1190
12. A.K. Jha, R. Batham, M. Ahmed, A.K. Majumder, O.P. Modi, S. Chaturvedi, and A.K. Gupta, Effect of Impinging Angle and Rotating Speed on Erosion Behavior of Aluminum, *Trans. Non-ferrous Met. Soc.*, 2011, **21**, p 32-38
13. B.F. Levin, J.N. Dupont, and A.R. Marder, Weld Overlay Coatings for Erosion Control, *Wear*, 1995, **181-183**(2), p 810-820
14. K.S. Tan, R.J.K. Wood, and K.R. Stokes, The Slurry Erosion Behaviour of High Velocity Oxy-Fuel (HVOF) Sprayed Aluminium Bronze Coatings, *Wear*, 2003, **255**, p 195-205
15. H.S. Grewal, S. Bhandari, and H. Singh, Parametric study of Slurry-Erosion of Hydroturbine Steels with and Without Detonation Gun Spray Coatings Using Taguchi Technique, *Metall. Mater. Trans. A*, 2012, **43**(9), p 3387-3401
16. B.S. Mann, High-Energy Particle Impact Wear Resistance of Hard Coatings and Their Application in Hydroturbines, *Wear*, 2000, **237**, p 140-146
17. J.F. Santa, J.C. Baena, and A. Toro, Slurry Erosion of Thermal Spray Coatings and Stainless Steels for Hydraulic Machinery, *Wear*, 2007, **263**(1-6), p 258-264
18. J.F. Santa, L.A. Espitia, J.A. Blanco, S.A. Romo, and A. Toro, Slurry and Cavitation Erosion Resistance of Thermal Spray Coatings, *Wear*, 2009, **267**(1-4), p 160-167
19. P. Singh, A. Bansal, and D.K. Goyal, Erosion wear Evaluation of HVOF Sprayed WC-12Co Coating on Some Pipeline Materials Using Taguchi Approach, *Kovove Mater.*, 2019, **57**, p 113-120
20. H.M. Clark, H.M. Hawthorne, and Y. Xie, Wear Rates and Specific Energies of Some Ceramic, Cermet and Metallic Coatings Determined in the Coriolis Erosion Tester, *Wear*, 1999, **233-235**, p 319-327
21. W. Barthlott and C. Neinhuis, Purity of the Sacred Lotus, or Escape from Contamination in Biological Surfaces, *Planta*, 1997, **202**(1), p 1-8
22. Y. Siab and Z. Guo, Superhydrophobic Nanocoatings: from Materials to Fabrications and to Applications, *Nanoscale*, 2015, **7**, p 5922-5946
23. I.P. Parkin and R.G. Palgrave, Self-cleaning Coatings, *J. Mater. Chem.*, 2005, **15**, p 1689-1695
24. B. Wu, M. Zhou, J. Li, X. Ye, G. Li, and L. Cai, Superhydrophobic Surfaces Fabricated by Microstructuring of Stainless Steel Using a Femtosecond Laser, *Appl. Surf. Sci.*, 2009, **256**, p 61-66
25. V.D. Ta, A. Dunn, T.J. Wasley, J. Li, R.W. Kay, J. Stringer, P.J. Smith, E. Esenturk, C. Connaughton, and J.D. Shephard, Laser Textured Superhydrophobic Surfaces and Their Applications for Homogeneous Spot Deposition, *Appl. Surf. Sci.*, 2016, **365**, p 153-159
26. B. Qian and Z. Shen, Fabrication of Superhydrophobic Surfaces by Dislocation-Selective Chemical Etching on Aluminum, Copper, and Zinc Substrates, *Langmuir*, 2005, **21**, p 9007-9009
27. Y. Xiu, Y. Liu, D.W. Hess, and C.P. Wong, Mechanically Robust Superhydrophobicity on Hierarchically Structured Si Surfaces, *Nanotechnology*, 2010, **21**, p 1-5
28. M. Morra, E. Occhiello, and F. Garbassi, Contact angle Hysteresis in Oxygen Plasma Treated Poly(tetrafluoroethylene), *Langmuir*, 1989, **5**, p 872-876
29. T. Darmanin and F. Guittard, Molecular Design of Conductive Polymers to Modulate Superoleophobic Properties, *J. Am. Chem. Soc.*, 2009, **131**, p 7928-7933
30. M.E. Buck, S.C. Schwartz, and D.M. Lynn, Superhydrophobic Thin Films Fabricated by Reactive Layer-by-layer Assembly of Azlactone-Functionalized Polymers, *Chem. Mater.*, 2010, **22**, p 6319-6327
31. A.M.A. Mohamed, A.M. Abdullah, and N.A. Younan, Corrosion Behavior of Superhydrophobic Surfaces: a Review, *Arab. J. Chem.*, 2015, **8**, p 749-765
32. A.M. Coclite, Y. Shi, and K.K. Gleason, Super-hydrophobic and Oleophobic Crystalline Coatings by Initiated Chemical Vapor Deposition, *Phys. Procedia*, 2013, **46**, p 56-61
33. D. Oner and T.J. McCarthy, Ultra-hydrophobic Surfaces: Effects of Topography Length Scales on Wettability, *Langmuir*, 2000, **16**, p 7777-7782
34. A. Pozzato, S.D. Zilio, G. Fois, D. Vendramin, G. Mistura, M. Belotti, Y. Chen, and M. Natali, Superhydrophobic Surfaces Fabricated by Nanoimprint Lithography, *Microelectron. Eng.*, 2006, **83**, p 884-888
35. P. Calcagnile, D. Fragouli, I.S. Bayer, G.C. Anyfantis, L. Martiradonna, P.D. Cozzoli, R. Cingolani, and A. Athanassiou, Magnetically Driven Floating Foams for the Removal of Oil Contaminants from Water, *ACS Nano*, 2012, **6**(6), p 5413-5419
36. K. Tsougeni, D. Papageorgiou, A. Tserepi, and E. Gogolides, Smart Polymeric Microfluidics Fabricated by Plasma Processing: Controlled Wetting, Capillary Filling and Hydrophobic Valving, *Lab Chip*, 2010, **10**, p 462-469
37. A. Milionis, E. Loth, and I.S. Bayer, Recent Advances in the Mechanical Durability of Superhydrophobic Materials, *Adv. Colloid Interface Sci.*, 2016, **229**, p 57-79
38. T. Verho, C. Bower, P. Andrew, S. Franssila, O. Ikkala, and R.H.A. Ras, Mechanically Durable Superhydrophobic Surfaces, *Adv. Mater.*, 2011, **23**, p 673-678
39. X. Chen, Y. Gong, X. Suo, J. Huang, Y. Liu, and H. Li, Construction of Mechanically Durable Superhydrophobic Surfaces by Thermal Spray Deposition and Further Surface Modification, *Appl. Surf. Sci.*, 2015, **356**, p 639-644
40. X. Chen, Y. Gong, D. Li, and H. Li, Robust and Easy-Repairable Superhydrophobic Surfaces with Multiple Length-Scale Topography Constructed by Thermal Spray Route, *Colloids Surf. A Physicochem. Eng. Asp.*, 2016, **492**, p 19-25
41. S. Jones, T.A. Stolarski, and S. Tobeb, Sliding Performance of Binary Metal-PTFE Coatings, *Wear*, 2004, **257**, p 539-554
42. H. Wang, E. Chen, X. Jia, L. Liang, and Q. Wang, Superhydrophobic Coatings Fabricated with Polytetrafluoroethylene and SiO₂ Nanoparticles by Spraying Process on Carbon Steel Surfaces, *Appl. Surf. Sci.*, 2015, **349**, p 724-732
43. S.W. Lee, J.W. Hong, M.Y. Wye, J.H. Kim, H.J. Kang, and Y.S. Lee, Surface Modification and Adhesion Improvement of PTFE Film by Ion Beam Irradiation, *Nucl. Instrum. Methods Phys. Res. B*, 2004, **219-220**, p 963-967
44. B.K. Sreedhar, S.K. Albert, and A.B. Pandit, Improving Cavitation Erosion Resistance of Austenitic Stainless Steel in Liquid Sodium by Hardfacing—Comparison of Ni and Co Based Deposits, *Wear*, 2015, **342-343**, p 92-99
45. H.S. Grewal, H. Singh, and A. Agrawal, Microstructural and Mechanical Characterization of Thermal Sprayed Nickel-Alumina Composite Coatings, *Surf. Coat. Technol.*, 2013, **216**, p 78-92
46. M.A. Nilsson, R.J. Daniello, and J.P. Rothstein, A Novel and Inexpensive Technique for Creating Superhydrophobic Surfaces Using Teflon and Sandpaper, *J. Phys. D Appl. Phys.*, 2010, **43**, p 1-12
47. J.K.N. Murthy, D.S. Rao, and B. Venkataraman, Effect of Grinding on the Erosion Behaviour of a WC-Co-Cr Coating Deposited by HVOF and Detonation Gun Spray Processes, *Wear*, 2001, **249**, p 592-600
48. I. Finnie, Some Reflections on the Past and Future of Erosion, *Wear*, 1995, **186-187**, p 1-10
49. I. Finnie, Erosion of Surfaces by Solid Particles, *Wear*, 1960, **3**(2), p 87-103

50. M. Hadad, R. Hitzek, P. Buergler, L. Rohr, and S. Siegmann, Wear Performance of Sandwich Structured WC-Co-Cr Thermally Sprayed Coatings Using Different Intermediate Layers, *Wear*, 2007, **263**, p 691-699
51. A. Marmur, Soft Contact: Measurement and Interpretation of Contact Angles, *Soft Matter*, 2006, **2**, p 12-17
52. L. Li, S. Roethel, V. Breedveld, and D.W. Hess, Creation of Low Hysteresis Superhydrophobic Paper by Deposition of Hydrophilic Diamond-like Carbon Films, *Cellulose*, 2013, **20**, p 3219-3226
53. M.A. Jaswin and D.M. Lal, Optimization of the Cryogenic Treatment Process for En 52 valve Steel Using the Grey-Taguchi Method, *Mater. Manuf. Process.*, 2010, **25**, p 842-850
54. A. Elkholy, Prediction of Abrasion Wear for Slurry Pump Materials, *Wear*, 1983, **84**, p 39-49
55. D.K. Goyal, H. Singh, and H. Kumar, An Overview of Slurry Erosion Control by the Application of High Velocity Oxy Fuel Sprayed Coatings, *J. Eng. Tribol.*, 2011, **225**, p 1092-1105
56. D.W. Wheeler and R.J.K. Wood, Erosion of Hard Surface Coatings for Use in Offshore Gate Valves, *Wear*, 2005, **258**, p 526-536
57. D.J. O'Flynn, M.S. Bingley, M.S.A. Bradley, and A.J. Burnett, A Model to Predict the Solid Particle Erosion Rate of Metals and its Assessment Using Heat-Treated Steels, *Wear*, 2001, **248**, p 162-177
58. T. Manisekaran, M. Kamaraj, S.M. Sharrif, and S.V. Joshi, Slurry Erosion Studies on Surface Modified 13Cr-4Ni Steels: Effect of Angle of Impingement and Particle Size, *J. Mater. Eng. Perform.*, 2007, **16**, p 567-572
59. D.A. Stewart, P.H. Shipway, and D.G. McCartney, Microstructural Evolution in Thermally Sprayed WC-Co Coatings: Comparison Between Nano Composite and Conventional Starting Powders, *Acta Mater.*, 2000, **48**, p 1593-1604
60. T. Sudaprasert, P.H. Shipway, and D.G. McCartney, Sliding Wear Behaviour of HVOF Sprayed WC-Co Coatings Deposited with Both Gas-Fuelled and Liquid-Fuelled Systems, *Wear*, 2003, **255**, p 943-949
61. A.J. Ninham and A.V. Levy, The Erosion of Carbide-Metal Composites, *Wear*, 1988, **121**, p 347
62. M.G. Gee, R.H. Gee, and I. McNaught, Stepwise Erosion as a Method for Determining the Mechanisms of Wear in Gas Borne Particulate Erosion, *Wear*, 2003, **255**, p 44-54
63. C. Verdon, A. Karimi, and J.L. Martin, Microstructural and Analytical Study of Thermally Sprayed WC-Co Coatings in Connection with Their Wear Resistance, *Mater. Sci. Eng. A*, 1997, **234**, p 731-734
64. L. Thakur and N. Arora, A Comparative Study on Slurry and Dry Erosion Behaviour of HVOF Sprayed WC-CoCr Coatings, *Wear*, 2013, **303**, p 405-411

Publisher's Note Springer Nature remains neutral with regard to jurisdictional claims in published maps and institutional affiliations.